REPORT DOCUMENTATION PAGE	Form Approved OMB NO. 0704-0188

1. REPORT DATE (DD-MM-YYYY) 09-12-2014	2. REPORT TYPE Final Report	3. DATES COVERED (From - To) 24-Sep-2012 - 24-Sep-2014

4. TITLE AND SUBTITLE Final Report: Turbulence Fine Structure, Intermittency, and Large-Scale Interactions in the Stable Boundary Layer and Residual Layer: Correlative High-Resolution Measurements and Direct Numerical Simulations	5a. CONTRACT NUMBER
	5b. GRANT NUMBER W911NF-12-C-0097
	5c. PROGRAM ELEMENT NUMBER 611102
6. AUTHORS David C. Fritts, Ben B. Balsley, Dale A. Lawrence	5d. PROJECT NUMBER
	5e. TASK NUMBER
	5f. WORK UNIT NUMBER
7. PERFORMING ORGANIZATION NAMES AND ADDRESSES G & A Technical Software, Inc. (GATS) 11864 Canon Blvd. Suite 101 Newport News, VA 23606 -4253	8. PERFORMING ORGANIZATION REPORT NUMBER
9. SPONSORING/MONITORING AGENCY NAME(S) AND ADDRESS (ES) U.S. Army Research Office P.O. Box 12211 Research Triangle Park, NC 27709-2211	10. SPONSOR/MONITOR'S ACRONYM(S) ARO
	11. SPONSOR/MONITOR'S REPORT NUMBER(S) 62311-EV.7

12. DISTRIBUTION AVAILIBILITY STATEMENT

Approved for Public Release; Distribution Unlimited

13. SUPPLEMENTARY NOTES

The views, opinions and/or findings contained in this report are those of the author(s) and should not contrued as an official Department of the Army position, policy or decision, unless so designated by other documentation.

14. ABSTRACT

The research employed stable boundary layer measurements using the DataHawk UAV and high-resolution direct numerical simulations (DNS) to examine the interactions and instabilities occurring in multi-scale flows that drive intermittent turbulence events in the stable atmosphere. Both measurements and the DNS revealed the occurrence and persistence of sheet-and-layer structures in the temperature and velocity fields that arise from, and drive, successive instabilities including Kelvin-Helmholtz instabilities (KHI), gravity wave breaking (GWB), and more

15. SUBJECT TERMS

stable boundary layer, multi-scale interactions, Kelvin-Helmholtz instabilities, gravity wave breaking, turbulence

16. SECURITY CLASSIFICATION OF:			17. LIMITATION OF ABSTRACT	15. NUMBER OF PAGES	19a. NAME OF RESPONSIBLE PERSON
a. REPORT	b. ABSTRACT	c. THIS PAGE			David Fritts
UU	UU	UU	UU		19b. TELEPHONE NUMBER 720-274-4747

Standard Form 298 (Rev 8/98)
Prescribed by ANSI Std. Z39.18

Report Title

Final Report: Turbulence Fine Structure, Intermittency, and Large-Scale Interactions in the Stable Boundary Layer and Residual Layer: Correlative High-Resolution Measurements and Direct Numerical Simulations

ABSTRACT

The research employed stable boundary layer measurements using the DataHawk UAV and high-resolution direct numerical simulations (DNS) to examine the interactions and instabilities occurring in multi-scale flows that drive intermittent turbulence events in the stable atmosphere. Both measurements and the DNS revealed the occurrence and persistence of sheet-and-layer structures in the temperature and velocity fields that arise from, and drive, successive instabilities including Kelvin-Helmholtz instabilities (KHI), gravity wave breaking (GWB), and more general fluid intrusions. Comparisons of measurements and modeling revealed many similarities and enabled an interpretation of a number of features of the observed flows. Also examined using the DNS results was the relationship between the Thorpe scale and the Ozmidov scale in such multi-scale flows. This revealed that the assumption that the ratio of these scales is approximately constant employed by many researchers is violated strongly on a case-by-case basis and may only be approximate for long spatial and temporal averages over turbulence events.

Enter List of papers submitted or published that acknowledge ARO support from the start of the project to the date of this printing. List the papers, including journal references, in the following categories:

(a) Papers published in peer-reviewed journals (N/A for none)

Received		Paper
12/05/2014	1.00	Ben B. Balsley, Dale A. Lawrence, Ronald F.Woodman, David C. Fritts. Fine-Scale Characteristics of Temperature,Wind,and Turbulence in the Lower Atmosphere (0–1,300 m)Over the South Peruvian Coast, Boundary-Layer Meteorology, (04 2013): 165. doi:
12/05/2014	2.00	David C. Fritts, Ling Wang, Joseph A. Werne. Gravity Wave–Fine Structure Interactions. Part I: Influences of Fine StructureForm and Orientation on Flow Evolution and Instability, Journal of the Atmospheric Sciences , (12 2013): 3710. doi:
12/05/2014	3.00	David C. Fritts, Ling Wang. Gravity Wave–Fine Structure Interactions. Part II: Energy Dissipation Evolutions,Statistics, and Implications, Journal of the Atmospheric Sciences, (12 2013): 3735. doi:
12/05/2014	4.00	David C. Fritts, Gerd Baumgarten, Kam Wan, Joseph Werne, and Tom Lund. Quantifying Kelvin-Helmholtz instability dynamicsobserved in noctilucent clouds: 2. Modelingand interpretation of observations, Journal of Geophysical Research, (08 2014): 9359. doi:

TOTAL: 4

Number of Papers published in peer-reviewed journals:

(b) Papers published in non-peer-reviewed journals (N/A for none)

Received	Paper

TOTAL:

Number of Papers published in non peer-reviewed journals:

(c) Presentations

1. Gravity Wave-Fine Structure Interactions and Effects in the MLT, Small-Scale Dynamics at Polar Latitudes, Utah State University, October 2012

2. Multi-Scale Gravity Wave Dynamics in the MLT, Fall AGU, 2012

3. Multi-Scale Gravity Wave and Instability Dynamics in the Atmosphere, CEDAR Workshop, June 2013

4. Instability Dynamics in Multi-Scale Flows, CEDAR Workshop, June 2013

5. Instabilities and Turbulence Arising from Multi-Scale Gravity Wave Interactions, EGU, Vienna, April 2013

6. Turbulence sources, character, and effects in the stable boundary layer: Insights from multi-scale direct numerical simulations and new, high-resolution measurements, EGU, Vienna, April 2013

7. Multi-Scale Interactions in the Atmosphere - Observations and Modeling, ALOMAR 20th Anniversary Symposium, Andoya, Norway, August, 2014

8. Modeling Gravity Wave Dynamics in the Middle Atmosphere, NCAR symposium, January 2014

Number of Presentations: 8.00

Non Peer-Reviewed Conference Proceeding publications (other than abstracts):

Received	Paper

TOTAL:

Number of Non Peer-Reviewed Conference Proceeding publications (other than abstracts):

Peer-Reviewed Conference Proceeding publications (other than abstracts):

Received		Paper
TOTAL:		

Number of Peer-Reviewed Conference Proceeding publications (other than abstracts):

(d) Manuscripts

Received		Paper
12/05/2014	5.00	Ben B. Balsley, Dale A. Lawrence, David C. Fritts, Ling Wang, Kam Wan. Fine Structure, Instabilities, and Turbulence in the Stable Boundary Layer, Part 1: High-Resolution In-Situ Measurements with the DataHawk UAV and Comparisons with Numerical Modeling , Journal of the Atmospheric Sciences (10 2014)
12/05/2014	6.00	David C. Fritts, Ling Wang, Kam Wan, Marvin A. Geller, Dale A. Lawrence, Joe Werne, Ben B. Balsley. Fine Structure, Instabilities, and Turbulence in the Stable Boundary Layer, Part 2: Numerical Modeling of Multi-Scale Interactions at High Reynolds Numbers, Journal of the Atmospheric Sciences (10 2014)
TOTAL:		**2**

Number of Manuscripts:

Books

Received		Book
TOTAL:		

Received Book Chapter

TOTAL:

Patents Submitted

Patents Awarded

Awards

Highly Cited researcher, upper 0.5%, by ISIHighlyCited since 2003

Graduate Students

NAME	PERCENT_SUPPORTED
FTE Equivalent:	
Total Number:	

Names of Post Doctorates

NAME	PERCENT_SUPPORTED
FTE Equivalent:	
Total Number:	

Names of Faculty Supported

NAME	PERCENT_SUPPORTED	National Academy Member
Ben B. Balsley	0.05	
Dale A. Lawrence	0.05	
FTE Equivalent:	**0.10**	
Total Number:	**2**	

Names of Under Graduate students supported

NAME	PERCENT_SUPPORTED
FTE Equivalent:	
Total Number:	

Student Metrics

This section only applies to graduating undergraduates supported by this agreement in this reporting period

The number of undergraduates funded by this agreement who graduated during this period: ......

The number of undergraduates funded by this agreement who graduated during this period with a degree in science, mathematics, engineering, or technology fields:......

The number of undergraduates funded by your agreement who graduated during this period and will continue to pursue a graduate or Ph.D. degree in science, mathematics, engineering, or technology fields:......

Number of graduating undergraduates who achieved a 3.5 GPA to 4.0 (4.0 max scale):......

Number of graduating undergraduates funded by a DoD funded Center of Excellence grant for Education, Research and Engineering:......

The number of undergraduates funded by your agreement who graduated during this period and intend to work for the Department of Defense ......

The number of undergraduates funded by your agreement who graduated during this period and will receive scholarships or fellowships for further studies in science, mathematics, engineering or technology fields: ......

Names of Personnel receiving masters degrees

NAME

Total Number:

Names of personnel receiving PHDs

NAME

Total Number:

Names of other research staff

NAME	PERCENT_SUPPORTED

FTE Equivalent:
Total Number:

Sub Contractors (DD882)

1 a. University of Colorado - Boulder

1 b. 3100 Marine Street

Boulder CO 803031058

Sub Contractor Numbers (c): GATS_SC-12004

Patent Clause Number (d-1): 52.227.11

Patent Date (d-2):

Work Description (e): CU performed all DataHawk developments and measurements. They also assisted with D

Sub Contract Award Date (f-1): 9/20/12 12:00AM

Sub Contract Est Completion Date(f-2): 9/19/14 12:00AM

1 a. University of Colorado - Boulder

1 b. 3100 Marine Street
Room 481
Boulder CO 803090572

Sub Contractor Numbers (c): GATS_SC-12004

Patent Clause Number (d-1): 52.227.11

Patent Date (d-2):

Work Description (e): CU performed all DataHawk developments and measurements. They also assisted with D

Sub Contract Award Date (f-1): 9/20/12 12:00AM

Sub Contract Est Completion Date(f-2): 9/19/14 12:00AM

Inventions (DD882)

Scientific Progress

See Attachment

Technology Transfer

Final Report for ARO Contract W911NF-12-C-0097

"Turbulence Fine Structure, Intermittency, and Large-Scale Interactions in the Stable Boundary Layer and Residual Layer: Correlative High-Resolution Measurements and Direct Numerical Simulations"

PI: D. C. Fritts (with Co-Is Ben Balsley and Dale Lawrence)

Date: 6 December 2014

Period of Performance: 20 September 2012 to 19 September 2014

1. Foreward

This document is a final report on ARO Contract W911NF-12-C-0097, entitled "Turbulence Fine Structure, Intermittency, and Large-Scale Interactions in the Stable Boundary Layer and Residual Layer: Correlative High-Resolution Measurements and Direct Numerical Simulations". It reports on two years of research employing both high-resolution in-situ measurements using a new, small, and versatile DataHawk UAV and correlative numerical modeling employing high-resolution direct numerical simulations (DNS) able to resolve multi-scale dynamics spanning scales from typical stable boundary layer depths into the viscous range of turbulence. Measurements were performed at a number of locations, in particular two locations in Peru and Dugway Proving Ground in Utah, and typically employed spiraling profiling to altitudes ranging from hundreds of meters to several km. New sensor technologies enabled high-resolution measurements of a number of key small-scale dynamics and turbulence parameters. Our DNS enabled computations of representative multi-scale flows that were able to describe much of the small-scale deterministic and statistical character various causes of sporadic turbulence. Comparisons of sampling of the DNS in a similar manner to the DataHawk sampling of the stable boundary layer yielded a number of insights into the typical instability sources of turbulence, turbulence intermittency and character, and the relations among various turbulence and background parameters. Our numerical studies also directly addressed the relation between the Thorpe and Ozmidov scales as a means of estimating turbulence intensities and mixing based on only vertical profiling of temperature. These efforts revealed this characterization of turbulence to be at best very approximate, and more typically very poorly motivated.

2. Table of Contents

1. Foreward 1
2. Table of Contents 1
3. List of Figures 2
4. Overview and Motivation for this Research 3
5. Important Results in SBL Measurements 4
    5.1 DataHawk flight and control modes 4
    5.2 DataHakw measurement sites 5
    5.3 DataHawk measurement examples 6
6. Important Results in Numerical Modeling 12
7. Important Results Comparing Measurements and Modeling 16
    7.1 New DNS results 16
    7.2 Vertical and slant-path sampling 17
8. Evaluation of the Thorpe/Ozmidov Scale Relation for Estimating ε 18
9. Bibliography: Publications Published, Submitted, and/or in Preparation 19

3. List of Figures

1. DataHawk on launch rails
2. Example DataHawk flight profile at Paracas, Peru
3. Example DataHawk flight profiles at Smoky Hills, Kansas
4. Example DataHawk wind, temperature, and humidity measurements at Paracas
5. Example C_T^2 profile at Jicamarca Radio Observatory (JRO)
6. Comparison of potential temperature (θ) and C_T^2 profiles at JRO
7. Comparison of C_T^2 and humidity (*q*) profiles at JRO
8. Flight geometry and profiles of θ, *d'*, L_T, L_O, L_T/L_O, *N*, ε, Re_b, C_T^2, *u* and *v*, du_h/dz, and *Ri* for the first flight on 11 October 2012 at DPG
9. As in Figure 8 for the second flight on 11 October 2012 at DPG
10. As in Figure 8 for the third flight on 11 October 2012 at DPG
11. Slant-path sampling of *u'*, *v'*, and θ' at a 1-s rate for the ascending and descending profiles for the first two flights at DPG on 11 October 2012
12. Profiles of non-dimensional θ, *u*, *v*, and *w* at the center of the computational domain from t = 0 to 24 T_b at intervals of 2 T_b for the DNS with linear and rotary fine-structure shears at *Re* = 50,000
13. 2D and 3D streamwise and vertical spectra for the DNS with linear and rotary fine-structure shears at *Re* = 50,000
14. Streamwise-vertical cross sections of spanwise-averaged $\log_{10}\langle\varepsilon\rangle$ at t = 10.5, 11, 11.5, 12, 12.5, and 13 T_b for the linear and rotary fine-structure shears at *Re* = 50,000
15. PDFs of $\log_{10}(\varepsilon)$ and $\log_{10}(Ri\ \chi)$ at t = 8 and 11.5 T_b subdomains of the DNS with linear and rotary fine-structure shears at *Re* = 50,000
16. Streamwise-vertical cross section of spanwise-mean $\log_{10}(\varepsilon)$ and $\log_{10}(Ri\ \chi)$ for the DNS with linear fine-structure shears at t = 11.5 T_b.
17. Domain mean ε and Re_b for the DNS at *Re* = 50,000 and 100,000 throughout the simulations.
18. Streamwise-vertical cross sections of the *u*, *w*, θ', and N^2 fields at t =10, 12, 14, and 16 T_b for the DNS at *Re* = 100,000
19. Vertical and slant-path profiles of θ, *d'*, L_T, log ε, *u* and *v*, and *Ri* from the DNS at *Re* = 100,000 displayed as vertical profiles
20. Slant-path profiles of θ', *u'*, and *v'*, from the DNS at *Re* = 100,000 for comparison with those obtained by the DataHawk at DPG
21. Streamwise-vertical cross sections of θ, N^2, ε, and $Ri\chi$ at left and *d'*, L_T, and L_O assuming smoothed and local ε at right at t=11.1 T_b for a GW breaking event in the DNS for *Re* = 100,000
22. As in Figure 21 for a KHI event and a fluid intrusion
23. Estimates of the mean ratio of Thorpe to Ozmidov scales, $C = L_T/L_O$, from 4-24T_b for the full domain and for each instability event assessed

4. Overview and Motivation for this Research

This report describes research performed under the above ARO contract throughout the 2-year follow-on to an initial contract to the PI at NWRA. Our efforts during this research addressed all four of the science goals related to characterization and understanding of turbulence sources, instability dynamics, their influences in multi-scale stable boundary layer flows, applications to the interpretation of high-resolution measurements using the DataHawk UAV, and implications for parameterization based on Thorpe and Ozmidov scale relations. During this time, we achieved major successes in both the observational and numerical modeling components of this study. These coordinated research efforts led to four papers published to date, two papers on comparisons of DataHawk measurements and supporting numerical modeling submitted, and two others in preparation. The scientific motivations for our research program are described below. Sections 5 to 8 describe in greater detail the observational and modeling results obtained, the inter-comparisons to date, assessments of parameterizations, and their implications for SBL dynamics.

Measurements performed during the CASES-99 field program and more recently demonstrated that the stable boundary layer (**SBL**) and the residual layer (**RL**) exhibit a wide range of dynamics on multiple scales. In particular, very high-resolution vertical profiling of winds and temperature has revealed that small-scale structure and turbulence are virtually always present. The sources and persistence of turbulence in stable or very stable atmospheric boundary layers have proven challenging to characterize because of the small scales and the very high-precision measurements required. Yet they are also critical to an improved understanding of SBL dynamics and their implications for transport of heat, momentum, and constituents, dispersion of plumes or contaminants, and the parameterization of these processes in large-scale, mesoscale, and numerical weather prediction (**NWP**) models, to cite a few examples.

Understanding state-of-the-art measurements in the SBL and RL is challenging because single-point measurements of any type often cannot distinguish spatial and temporal variations. Even with multiple such measurements, it is difficult to define all of the relevant spatial and temporal scales, to characterize the larger-scale environment fully, and to interpret observations unambiguously. But with multiple such measurements, coupled with suitable models of these SBL and RL dynamics providing a context within which to interpret the measurements, significant advances in understanding SBL and RL dynamics, mixing, and transport are likely. Indeed, there is considerable synergism between 1) measurements able to define SBL and RL temperature, wind, and turbulence profiles with high resolution and precision at multiple sites and 2) high-resolution direct numerical simulations (**DNS**) able to describe the larger-scale dynamics and their implications for instability and turbulence at smaller scales. This synergism provides a unique opportunity to advance our understanding of SBL and RL dynamics.

Specific goals of our SBL and RL research employing our combined measurement and modeling capabilities included the following:

1) ***characterization of the tendency for instability and turbulence in general multi-scale SBL and RL flows, and their respective time scales,***
2) ***understanding the instability dynamics that drive large- and small-scale turbulence, their scales, and their dependence on multi-scale environmental parameters,***
3) ***implications of these instability dynamics for mixing, dispersion, SBL and RL evolution, and subsequent instabilities and turbulence, and***
4) ***testing, and guidance for improving, parameterizations of the effects of these dynamical processes in large-scale models.***

5. Important Results in SBL Measurements

Results discussed here include observations performed in July 2011 in Paracas, Peru, in January 2012 at the Jicamarca Radio Observatory (JRO), Peru, and in October 2012 at Dugway Proving Ground (DPG), UT. Over the initial phase of our research, Co-I Ben Balsley (and CU colleague Dale Lawrence) incorporated numerous design changes, new instrumentation, and telemetry enhancements into our measurement systems. Following the unfortunate death of Ben Balsley, the PI and Dale Lawrence continued the collaboration with the same goals. Collectively, these efforts resulted in dramatically improved capabilities for high-resolution profiling of the SBL and RL, and to higher altitudes. Improvements to date employing a new airborne platform, the DataHawk, have been significant and include:

- Improved attitude and roll stability,
- Ground temperature sensor for BL thermal correlations,
- accurate in-flight temperature calibration with a very linear response (thermistor/cold wire),
- Humidity sensing that works very well,
- Completely autonomous operation, launch to landing,
- Broadband (cold-wire) turbulence (C_T^2) measurement capability with ~few m resolution,
- Extended-range telemetry capability to altitudes of 9 km,
- Development of a triple failsafe abort capability for flight safety,
- A balloon-launch capability for higher-altitude studies, and
- Developed a 2-scene capability for simultaneous flight monitoring & scientific evaluation.

The DataHawk that supports these capabilities is shown on its launch rails in Figure 1.

5.1. DataHawk flight and control modes

The measurement programs noted above also demonstrated several flight profiles that we used, and expect to use frequently, in future campaigns. Two employed for our earlier measurement in Peru are shown in Figure 2, and include 1) ascents or descents at prescribed rates of ± a few ms^{-1} and 2) constant-altitude flights for arbitrary intervals. Circular patterns can be flown either as 3) tight ascending or descending spirals or 4) broad, repeatable circles, as demonstrated during the recent measurements at DPG (see Figure 3).

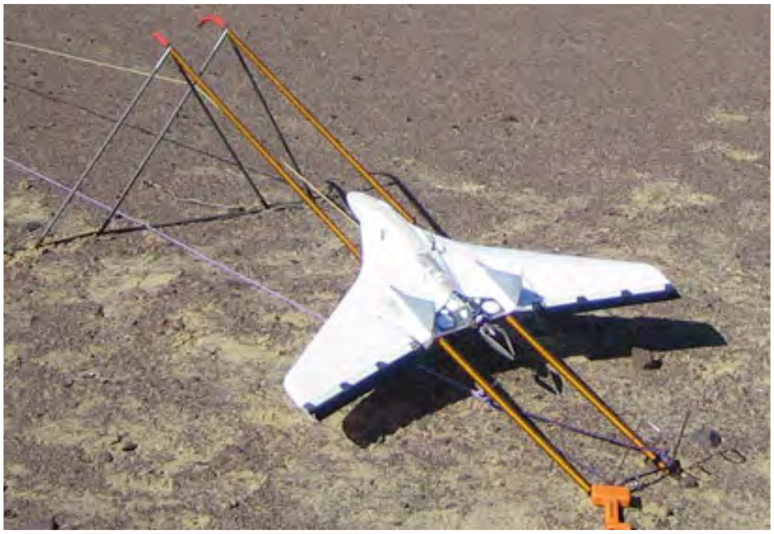

Figure 1. DataHawk on launch rails during field measurements in Paracas, Peru in July 2011.

Two-way telemetry enables both 1) monitoring and modifying the flight plan during the flight, and 2) viewing the down-linked data and flight information “on-line”. New high-gain, circularly-polarized, ground-based antennas also extend the DataHawk operating range to well over 10 km. These capabilities allow the DataHawk flights to be altered in flight, if interesting features warrant changes not anticipated in advance.

5.2. DataHawk measurement sites

The two sites used in the Peruvian campaigns are Paracas (a coastal site ~300 km south of Lima), and JRO in the Andean foothills. Paracas is almost an unoccupied desert location, while JRO is the site of a well-known atmosphere-ionosphere observatory containing the world’s largest antenna, along with a number of additional atmospheric radars. Relative to existing sites in the US, the two Peruvian locations provide significant advantages for the specific SBL and RL studies relevant to our ARO funding.

5.2.1. Paracas

Paracas provides the following attributes and advantages relative to Smoky Hill and/or DPG:

- No site costs (compared with Smoky Hill @ $3k/2 days and DPG @ $10k/campaign)
- Virtually constant acceptable weather conditions (no rain, no storms, no winter)
- Ideal, predictable, perennial wind conditions (minimal nighttime and morning winds)
- Very cooperative, essentially “on-line”, arrangements with the local FAA (CORPAC)
- The existence of a semi-permanent, very steep temperature gradient topping the ABL that arises from the combination of the cold Pacific ocean and the warm tropical atmosphere.

5.2.2. JRO

Advantages for JRO are nearly identical to those for Paracas, except that the temperature gradient is somewhat less steep, and the wind conditions a bit more variable. An additional JRO feature is the existence of the radar facility and the associated radar expertise. Moreover, the over-arching Peruvian Geophysical Institute (IGP) now operates a boundary layer radar (BLR) in northern Peru, and we are discussing the possibility of transferring it to JRO specifically for cooperative studies with our DataHawk capabilities.

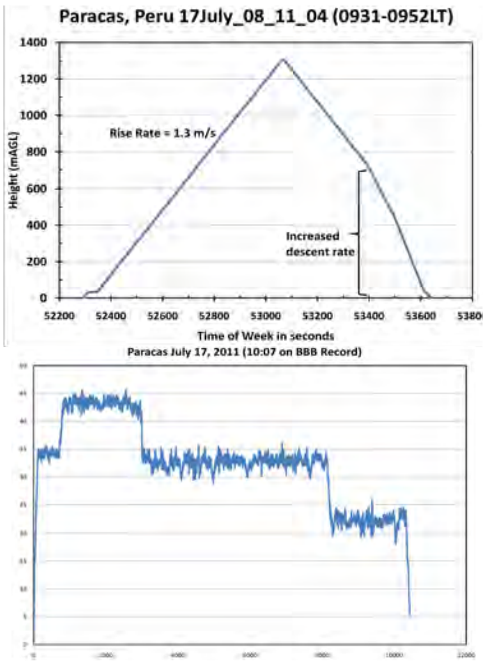

Figure 2. DataHawk profiles showing constant ascent/descent and constant altitude capabilities (top and bottom).

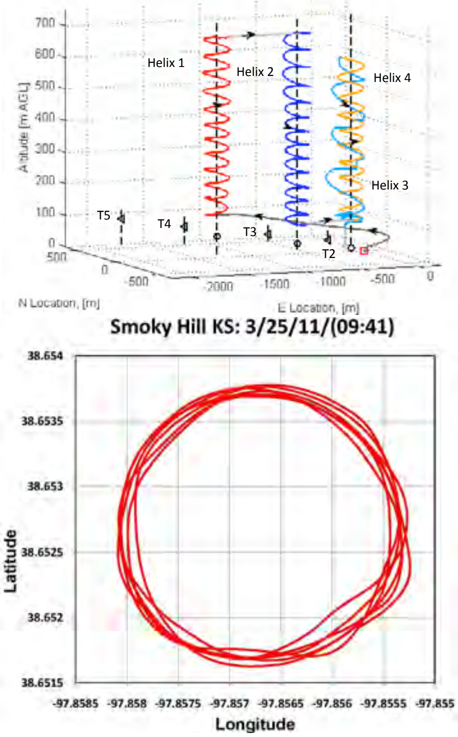

Figure 3. Large and small spiral profiles ascending/descending or at a constant altitude at DPG and Smoky Hills, Kansas.

With these advantages, and considering the presence of the nearly permanent temperature gradient topping the ABL 24 hr/day, it is clear that Paracas and JRO provide ideal and unique laboratories for ongoing ABL high-resolution research. Data from our initial measurement program demonstrating the synergism between our *in situ* measurements and the JRO SOUSY radar are shown in Figure 6 below. These reveal, as seen in other lower-resolution measurements, that T' variance and C_T^2 correlate very well with highly stable, layers rather than the more nearly neutrally-stable layers that appear to have evolved from previous turbulence events.

5.3. DataHawk measurement examples

5.3.1. Paracas measurements

We review below the various measurement capabilities and contributions to date performed with the DataHawk. The initial measurements performed in Paracas were also reported by Balsley et al. (2013).

5.3.1.a. Temperature and potential temperature profiles

Figure 4 (top) shows an example of a high-resolution temperature profile from the surface to 1300 m. This profile illustrates the steep temperature inversion routinely found at Paracas and likely constitutes a region of enhanced small-scale dynamics and an ideal laboratory for multi-scale interactions. Modeling and theory suggest that strong inversions should be preferred sites for multi-scale dynamics, instabilities, and intermittent turbulence events, and the potential temperature profile and fluctuations about the mean corresponding to the temperature field shown at top in Figure 4 are shown in the second panel.

The second panel of Figure 4 illustrates the capability of the DataHawk to resolve gravity wave (***GW***) temperature fluctuations at small amplitudes and vertical scales. Note the clear periodic nature of the GWs. These features are especially apparent in the steep temperature inversion, with very little evidence for such outside. These data suggest small-scale vertical structures consistent with the temperature measurements. However, *in-situ* measurements mix spatial and temporal scales, so

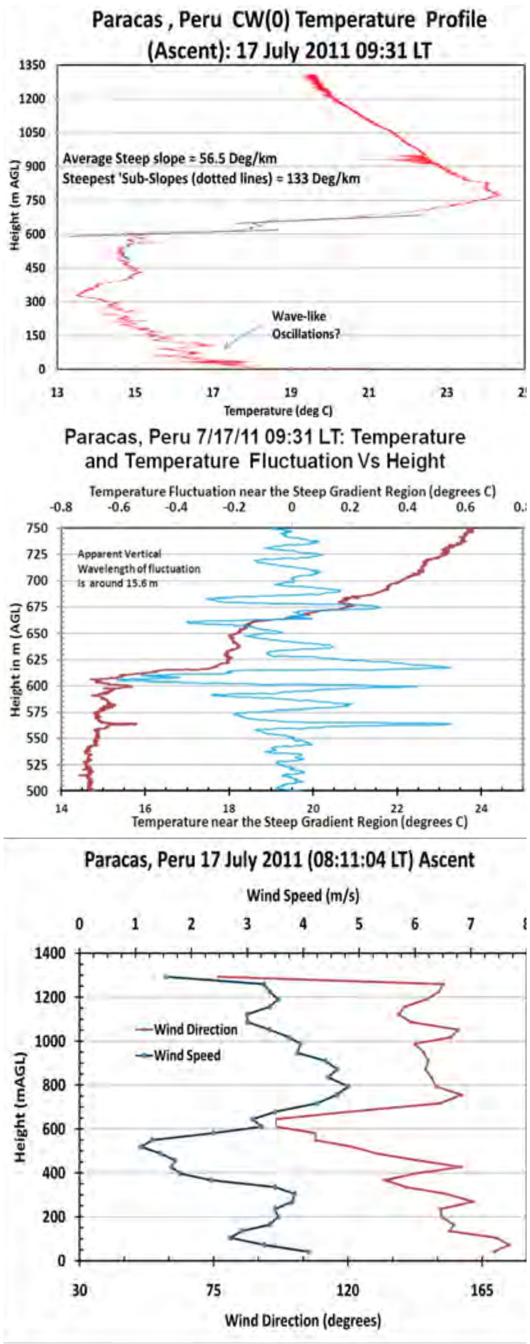

Figure 4. (top) High-resolution temperature profile showing a strong inversion and significant small-scale structures from 0 to ~1300 m. (second panel) Potential temperature profile (red) and fine-structure (blue) from 500 to 750 m. (third panel) Wind speed (blue) and direction (red) obtained from the DataHawk GPS positioning system computed during circling maneuvers.

future measurements will involve formation flying of several DataHawks to aid us in removing these ambiguities.

5.3.1.b. Wind measurements

Wind speed and direction determined from ascending helical circles measured simultaneously with the steep temperature gradient (e.g., Figure 3, top, and Figure 4, bottom) show pronounced variations in the region of the steep gradient. While these measurements provide reasonable ~100 m resolution of the 2D wind field, we also demonstrated the capability for much higher resolution measurements of horizontal winds in the recent measurements at DPG (see below).

5.3.1.c.High-resolution C_T^2measurements

Figure 5 shows the first C_T^2 profile obtained during the DataHawk test flights at Paracas, Peru. These reveal the enormous potential for this measurement technique with high sensitivity to small magnitudes even extending to higher altitudes.

5.3.2. JRO measurements

Initial measurements with the DataHawk at JRO in January 2012 enabled both characterization of the SBL structure over this site and a comparison of C_T^2 using DataHawk temperature measurements with radar backscatter using the SOUSY VHF radar that is known to rely on, and potentially be biased by, refractive index variations and their alignments that are dictated by the small-scale dynamics responsible for their presence. A comparison between these two fields is shown in Figure 6 and reveals close agreement between maxima in C_T^2 and potential temperature gradients that agree well with theory and modeling studies. A higher-altitude flight (to 3.6 km) yielded strong evidence of "sheet-and-layer" (S&L) structures that agreed extremely well between potential temperature (θ) and humidity (q) (Figure 7).

5.3.3. DPG measurements

Initial measurements with the DataHawk at DPG employed the measurement strategy shown in Figure 3. Successive ascending and descending profiles to ~700 m on 11 October 2012 were performed with spiraling flights allowing measurements of potential temperature, winds, and C_T^2 at sites spaced at up to ~1.5 km (see Figures 8 to 10). These revealed larger-scale flow depths of ~300 m (shown with red lines at upper left) and embedded smaller-scale features having typical depths of ~60 m.

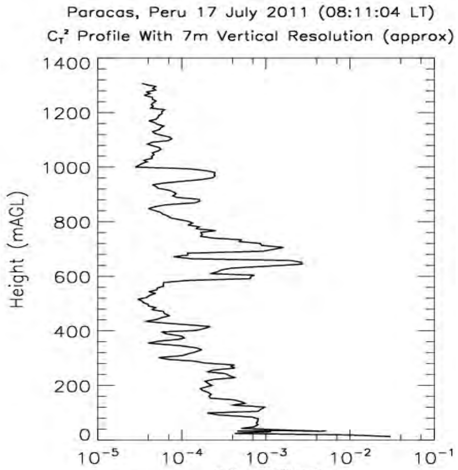

Figure 5. C_T^2 profile obtained from DataHawk T measurements for the flight shown at top in Figure 4.

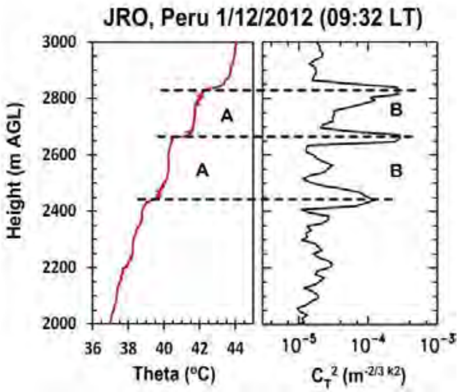

Figure 6. θ (left) and C_T^2 (right) from co-located DataHawk and SOUSY radar meas. at JRO.

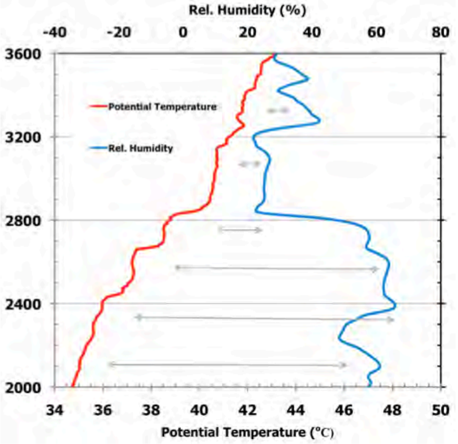

Figure 7. θ (left) and q (right) profiles measured on the higher-altitude at JRO.

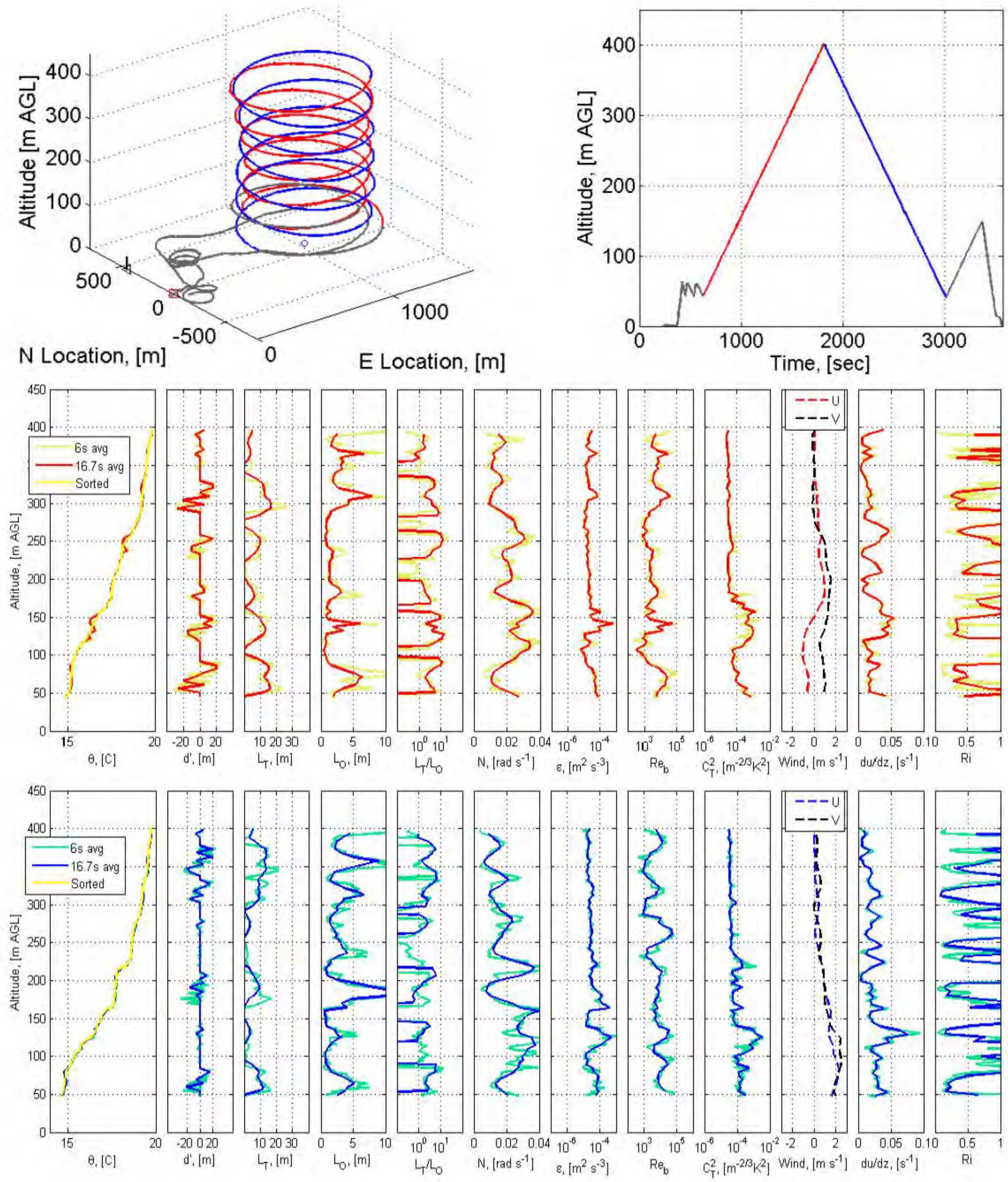

Figure 8. Flight 1 ascending and descending circular flight paths (top left) and altitude-time profile (top right) beginning at 07:58:17 LT on 11 October 2012. Profiles of θ, d', L_T, L_O, L_T/L_O, N, ε, Re_b, C_T^2, u and v, du_h/dz, and Ri for the ascending (middle) and descending (bottom) profile sets (color codes at left and top). (After Balsley et al. 2014.)

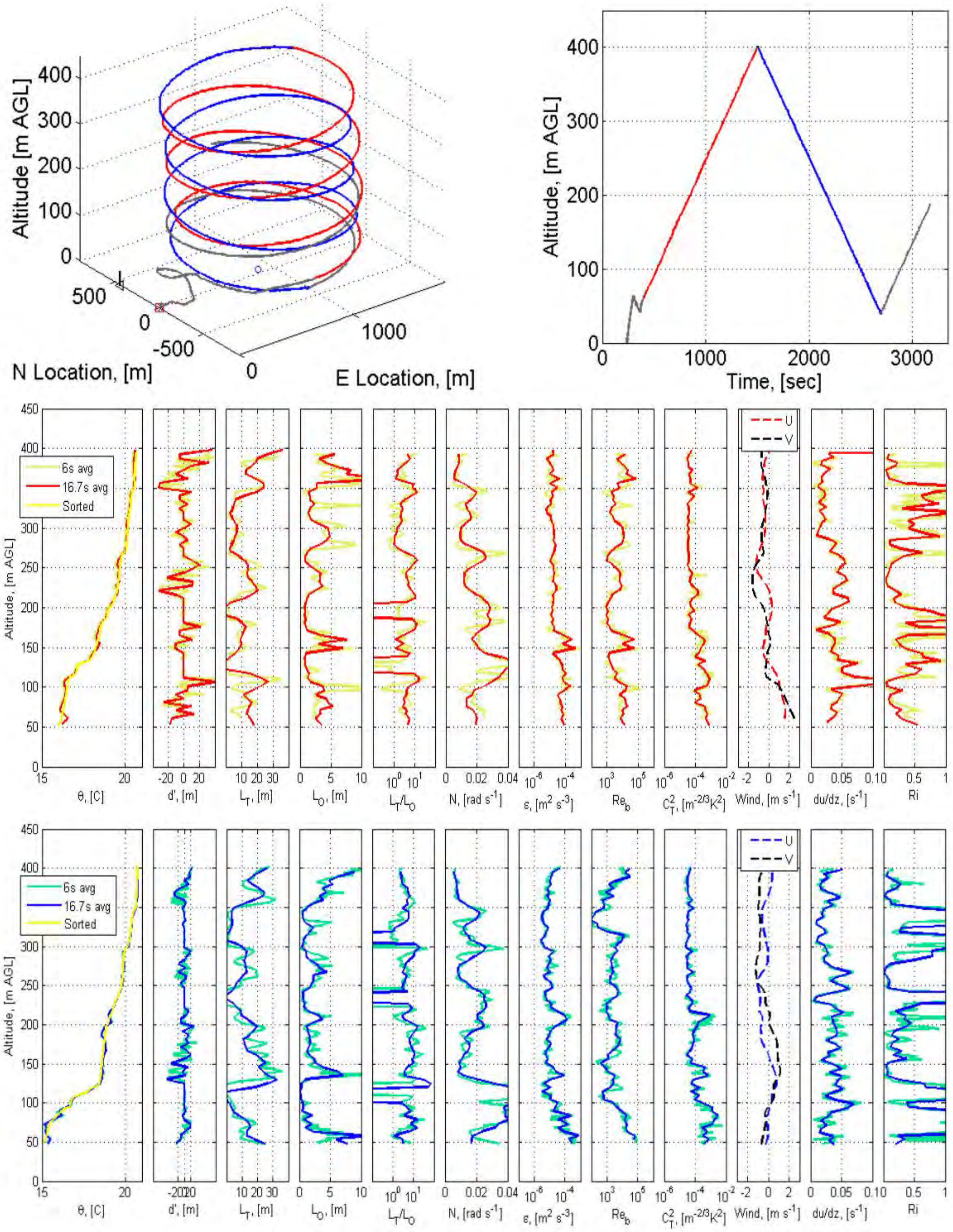

Figure 9. As in Figure 8 for Flight 2 beginning at 09:02:27 LT on 11 October 2012. (After Balsley et al. 2014.)

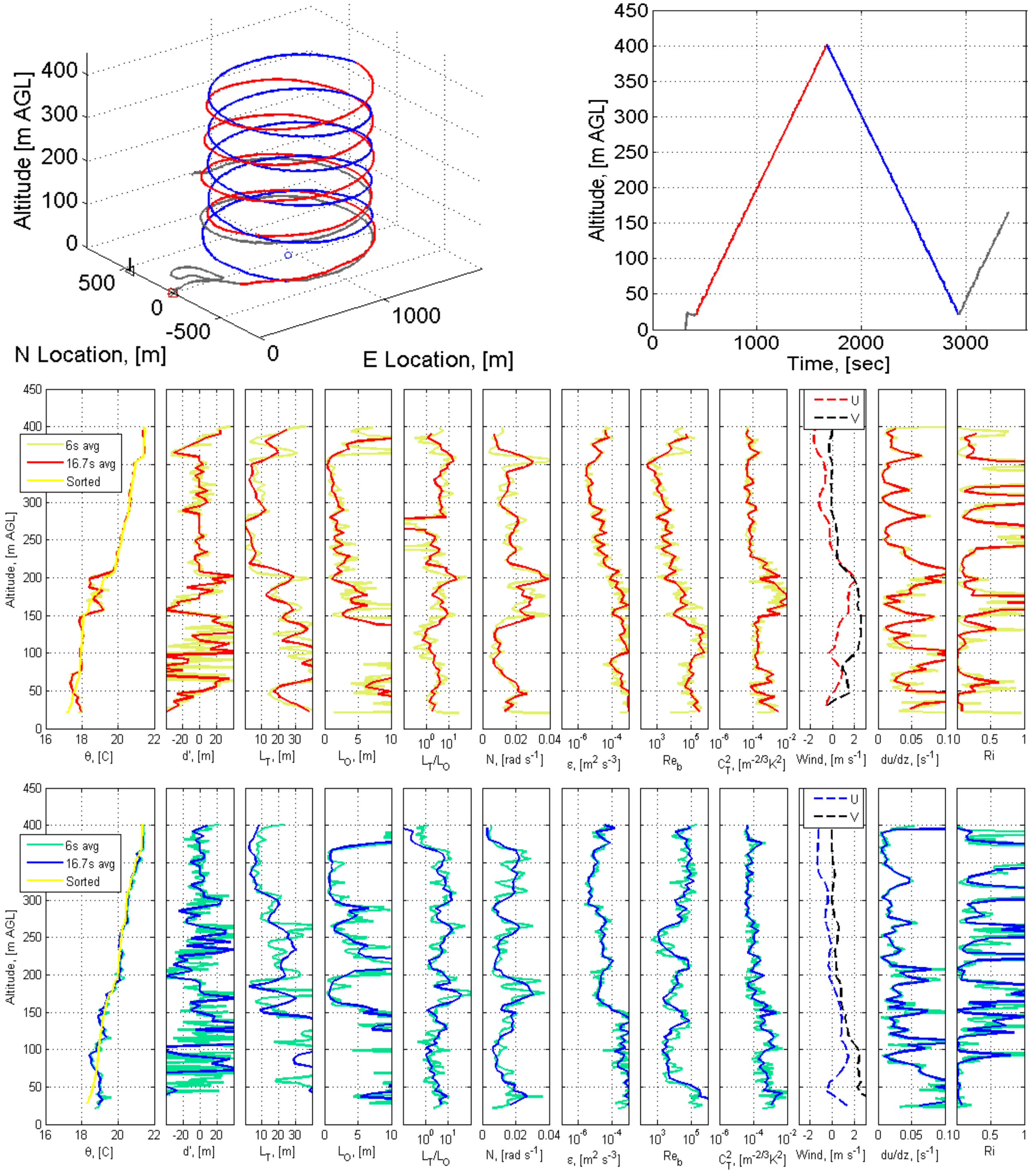

Figure 10. As in Figure 8 for Flight 3 beginning at 10:04:28 LT on 11 October 2012. (After Balsley et al. 2014.)

The initial estimates of energy dissipation rate, *ε*, and C_T^2 reveal high sensitivity to small magnitudes. Typical minimum and maximum values for *ε* are <10^{-5} and ~10^{-3} m^{2}s^{-3} above ~200 m. These results also show strong sensitivity to Thorpe and Ozmidov scales, and to the character of the instabilities leading to turbulence, as described below. (After Balsley et al. 2014.)

Because the spiraling DataHawk measurements are not true vertical profiles, there is a potential for apparent vertical gradients that are in fact horizontal gradients due to GW or instability features having relatively small horizontal scales. Thus, we also examined DPG DataHawk measurements of *θ*', *u*', and *v*' along slanted paths for comparisons with similar sampling of the DNS fields in the same manner. These are displayed for the first two flights in Figure 11 for comparisons with the DNS results discussed below.

Seen in Figure 11 are multiple cases where significant quasi-sinusoidal variations in either or both (*u*',*v*') and *θ*' fields occur. As described by Balsley et al. (2014), these exhibit various correlations that can be interpreted as different stages of GWs, Kelvin-Helmholtz instability (KHI), and/or evolving turbulence fields, and which greatly enhance the quantification of these data, and are features that cannot easily be diagnosed with true vertical sampling.

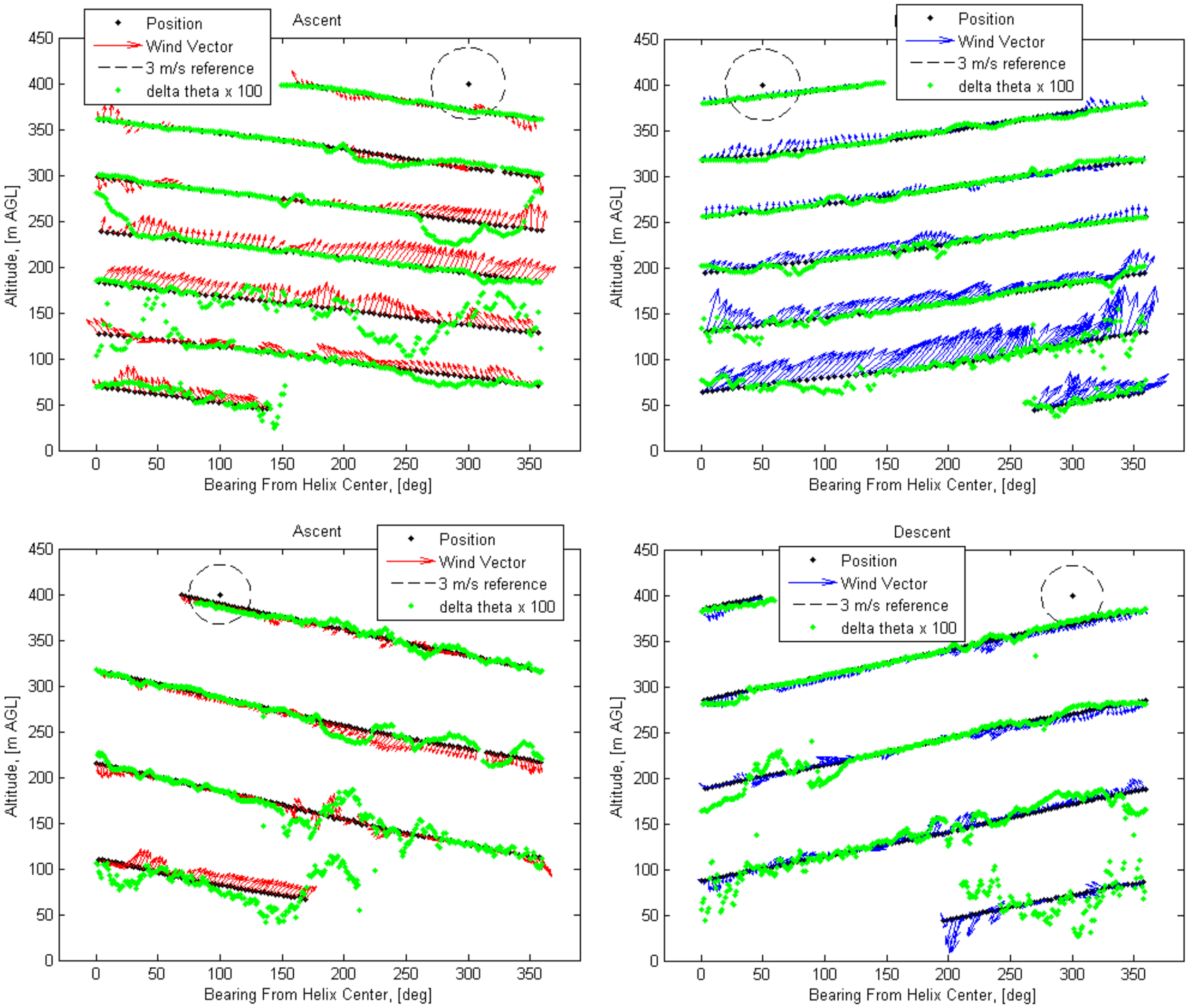

Figure 11. Horizontal velocity, (*u*',*v*'), and *θ*' (green, positive upward) perturbations at 1-s intervals for the ascending (left, red arrows) and descending (right, blue arrows) segments of Flights 1 and 2 (top and bottom) on 11 October 2012. All flight segments are counter-clockwise and velocity vectors are shown with north upward. Magnitudes are shown in the panel legends.

6. Important Results in Numerical Modeling

Modeling studies advanced dramatically throughout this research funding. Two publications resulting largely from these early efforts were published in the Journal of the Atmospheric Sciences, see Fritts et al. (2013) and Fritts and Wang (2013). Following modeling efforts extended the earlier studies for comparisons with DataHawk measurements performed in October 2012. These comparisons, and applications to an evaluation of the relation between the Thorpe and Ozmidov scales, are described in two additional papers recently submitted to the Journal of the Atmospheric Sciences, e.g., Balsley et al. (2014) and Fritts et al. (2014). The earlier results are summarized here; the latter modeling and comparisons with DataHawk measurements are described in the following sections.

We performed an initial suite of DNS of multi-scale interactions that we believe illustrate a range of SBL dynamics containing residual fine structure (***FS***) in the wind field due to previous mixing events and larger-scale GWs which interact and mutually deform each other. These studies included sinusoidal FS shears of $\boldsymbol{U_z} = \mathrm{d}U/\mathrm{d}z = 2N$, with $\boldsymbol{U}$ and $\boldsymbol{N}$ the local FS wind and buoyancy frequency (yielding an initial FS Richardson number of $\boldsymbol{Ri} = N^2/U_z^2 = 0.25$). Other parameters include a GW initial amplitude $\boldsymbol{a} = u'/(U\text{-}c) = 0.5$ (with u' and c the GW horizontal perturbation velocity amplitude and horizontal phase speed) a Reynolds number of $\boldsymbol{Re} = \lambda_z^2/T_b\nu = 50{,}000$, with $\boldsymbol{\lambda_z} = 2\pi/m_{GW}$ the GW vertical wavelength, $\boldsymbol{T_b} = 2\pi/N$ the buoyancy period, a GW period $\boldsymbol{T_{GW}} = 10\ T_b$, kinematic viscosity $\boldsymbol{\nu}$, and a FS wavenumber of $\boldsymbol{m_{FS}} = 5m_{GW}$. We also examine both streamwise linear and rotary (both streamwise and spanwise) FS forms in order to assess the sensitivity of instabilities and turbulence to FS form. The results of these DNS reveal high sensitivity of SBL turbulence evolutions to the details and intensities of the initial flow structures and orientations that will be described further below.

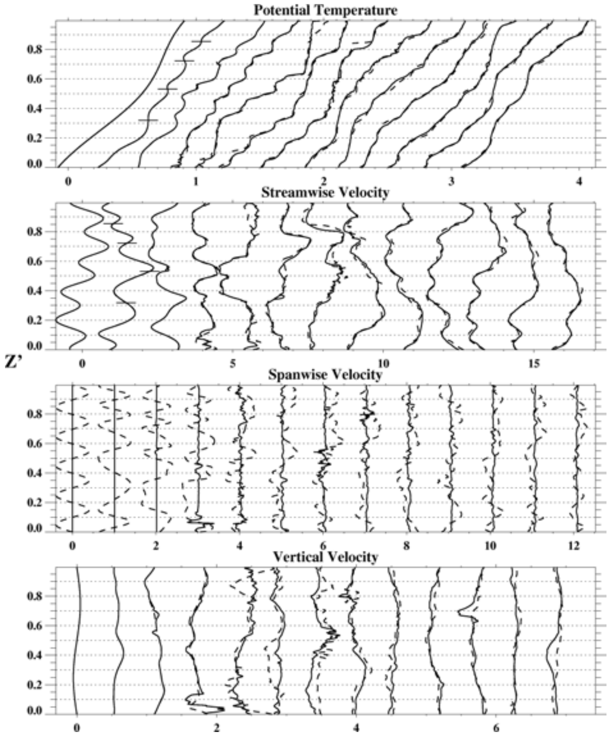

Figure 12. Profiles of non-dimensional θ (top) and u, v, and w (second to fourth panels) at the center of the computational domain from $t = 0$ to 24 T_b at intervals of 2 T_b. Cases L0 and R are shown with solid and dashed lines, respectively (after Fritts et al. 2013).

To illustrate the evolutions in a form that can be compared with DataHawk measurements, we show in Figure 12 the vertical profiles of potential temperature and the component velocities at 2 T_b intervals spanning 2.4 T_{GW}. Results for the linear and rotary FS forms are shown as solid and dashed lines, respectively. These reveal a close correspondence between the two evolutions, but with clear differences at smaller and larger scales that arise at different times due to the different turbulence transitions in each case. Both cases, however, exhibit many features that resemble closely these fields in the DataHawk measurements. These similarities include: 1) a superposition of velocities having larger and smaller vertical scales, 2) regions of apparent high small-scale variance suggesting localized strong turbulence events, and 3) the evolution of S&L structures in the potential temperature field as a consequence of larger-scale advection and local instability and turbulence.

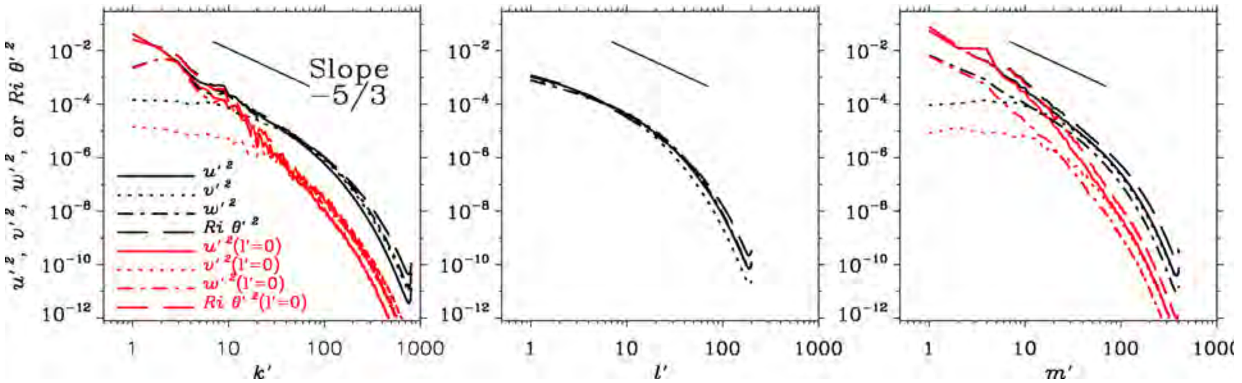

Figure 13. Domain-averaged component energy spectra of u', v', w', and $Ri\ \theta'$ versus k', l', and m' (left to right) for linear FS at $t = 11.5\ T_b$. 2D ($l' = 0$) and 3D ($l' \neq 0$) spectra are shown with red and black lines, respectively. Line codes are shown at upper left. Also shown in each panel is a spectral slope of -5/3 for reference. Rotary FS spectra are very similar.

The large-scale flows are very similar throughout the two evolutions, and these similarities are traced by Fritts et al. (2013) to the larger-scale wave-wave interactions driven by mutual deformation of the GW and FS fields. Indeed, it is these fields that drive instability and turbulence events throughout the two evolutions at smaller scales. These differences are especially apparent in potential temperature and component velocity spectra for the 2D (spanwise wavenumber = 0) and 3D (spanwise wavenumber ≠ 0) shown as red and black lines, respectively, for the linear FS in Figure 13.

There are, nevertheless, significant differences in the instability and turbulence fields that arise due to the linear and rotary FS forms. Their influences are illustrated in the energy dissipation rate fields at intermediate times in Figure 14. The reasons for these differences derive from the different growth rates and effects of different instability forms in the linear and rotary FS fields. The linear FS enables a streamwise-aligned instability analogous to a sheared convective boundary layer or the secondary instabilities in the outer portions of Kelvin-Helmholtz billows at small Richardson number. Spanwise FS disrupts these instabilities, however, reduces or eliminates their growth rates, and allows instead a distorted form of instability that evolves more slowly thereafter. The consequence is a delayed onset (by ~1-2 T_b) with rotary FS, relative to linear FS, depending on where in the flow these instabilities arise.

The different instability types and evolutions referred to above have some clear implications for atmospheric measurements of multi-scale dynamics using various *in-situ* and ground-based sensors. A convenient way to evaluate and describe the characteristics, statistics, and influences of instabilities and turbulence on the larger-scale flow is via probability distribution functions (PDFs) of various parameters. For example, theory anticipates that idealized turbulence should exhibit log-normal distributions of dissipation rates. Indeed, our previous DNS of individual GW breaking events did yield quasi-log-normal distributions for both ε and χ that survived to late times, though with decreasing magnitudes with time following the most intense turbulence.

In the DNS described here, however, there are multiple sources of turbulence at different times and locations and having different generation dynamics. Also, the mutual deformations of the GW and FS flows yield much stronger shearing than occurred prior to instability and turbulence in the earlier DNS.

To illustrate the evolutions of these fields for our DNS of multi-scale flows, we show in Figure 15 PDFs of $\log_{10}(\varepsilon)$ and $\log_{10}(Ri\ \chi)$ for subdomains of the overall DNS domain that each represent 10% increments of the total domain in the streamwise and vertical, and the full domain in the spanwise direction. Here, Ri is the bulk Richardson number that normalizes the contributions of each field to total energy dissipation. The upper three rows show the various PDFs in the upper 30% of the domain at t = 8 T_b prior to widespread small-scale instabilities; the lower rows show these PDFs in the same regions at t = 11.5 T_b following significant instabilities at multiple locations (see Figure 14).

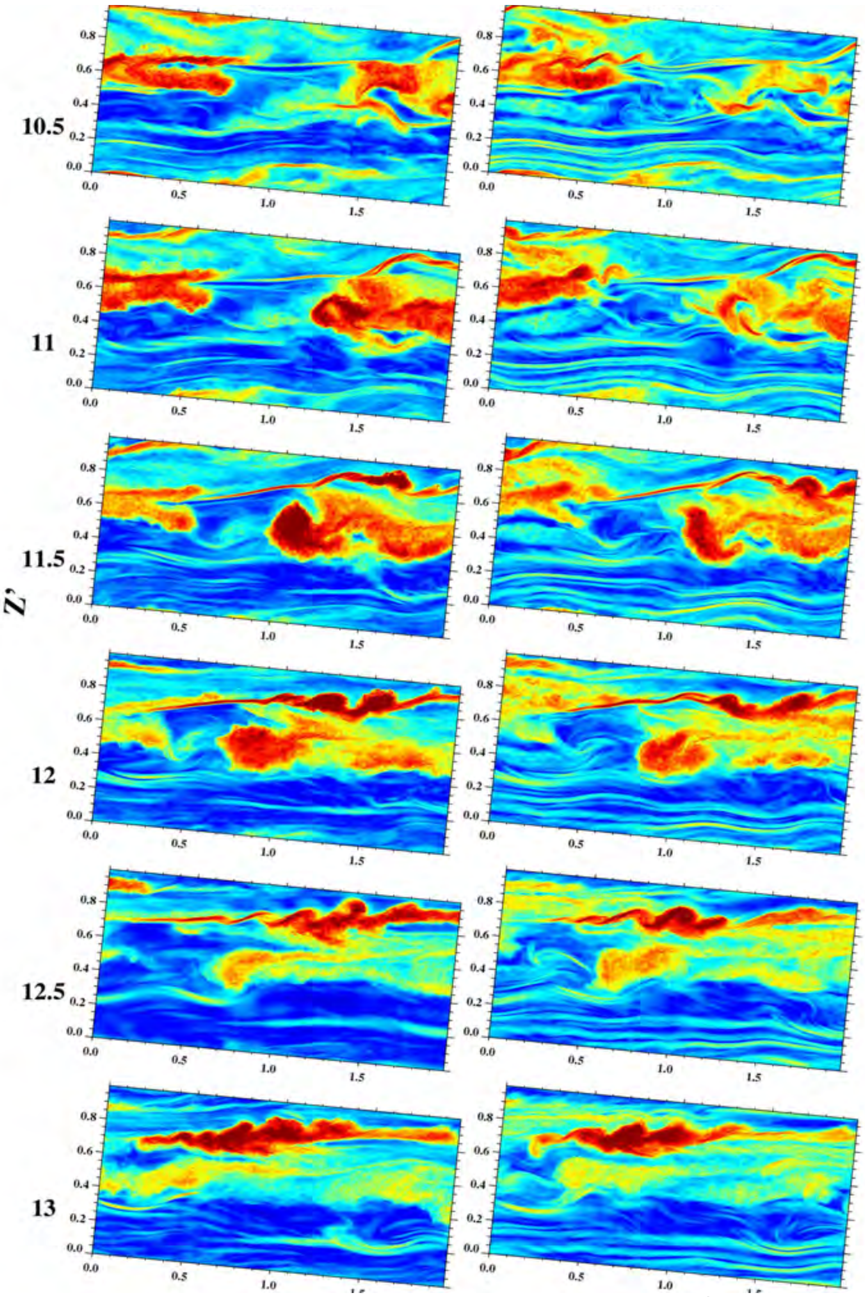

Figure 14. Streamwise-vertical cross sections of spanwise-averaged $\log_{10}\langle\varepsilon\rangle$ at t = 10.5, 11, 11.5, 12, 12.5, and 13 T_b for the linear and rotary FS (left and right). The color scale is the same for all panels and spans 5 decades of intensities.

The PDFs in Figure 15 exhibit various behaviors, depending on locations and times. The distributions are typically broad and quasi-log-normal where turbulence events are well developed. Prior to turbulence, however, both $\log_{10}(\varepsilon)$ and $\log_{10}(Ri\ \chi)$ PDFs exhibit sharp peaks and long tails, indicating high skewness and/or kurtosis. Those for the rotary FS often exhibit multiple peaks, suggesting multiple sharp sheets with differing intensities in a given sub-domain prior to turbulence. These are especially prevalent in the PDFs for the rotary FS, where spanwise FS delays initial instability transitions. Similar behavior is also seen, but now smoother, in the linear and rotary $\log_{10}(Ri\ \chi)$ PDFs at later times. In these cases, Fritts and Wang (2013) traced this behavior to strong turbulent mixing that acted to eradicate thermal gradients in these regions, reducing their intensities in $\log_{10}(Ri\ \chi)$ relative to $\log_{10}(\varepsilon)$, despite maintained large $\log_{10}(\varepsilon)$. A comparison of the spatial distributions of these two fields for the linear FS at t = 11.5 T_b is shown in Figure 16. These reveal "voids" in $\log_{10}(Ri\ \chi)$ where $\log_{10}(\varepsilon)$ remains large that may cause turbulence intensities to be unmeasurable in these regions, due to lack of refractive index fluctuations caused by eradication of these gradients in accompanying strong mixing.

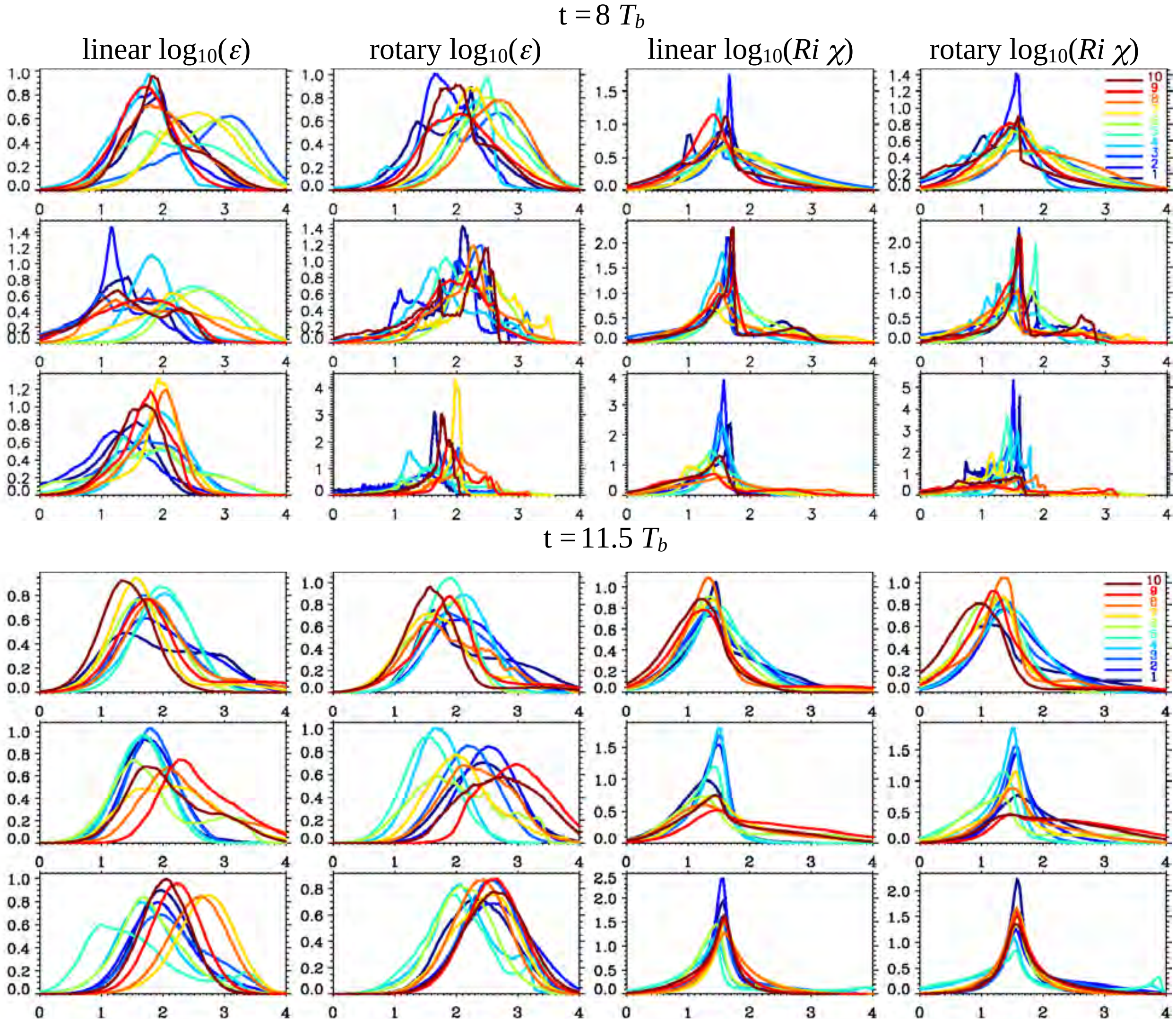

Figure 15. PDFs of $\log_{10}(\varepsilon)$ and $\log_{10}(Ri\ \chi)$ at t = 8 and 11.5 T_b (upper and lower rows) for 1/10th of the domain in the vertical (e.g., top 30% of the domain) and for each 1/10th of the domain in the horizontal (blue to red, see color coding at upper left). Left two (right two) columns show $\log_{10} \varepsilon$ ($\log_{10} Ri\ \chi$) for the linear (rotary) FS. The PDF magnitudes span 5 decades for all panels.

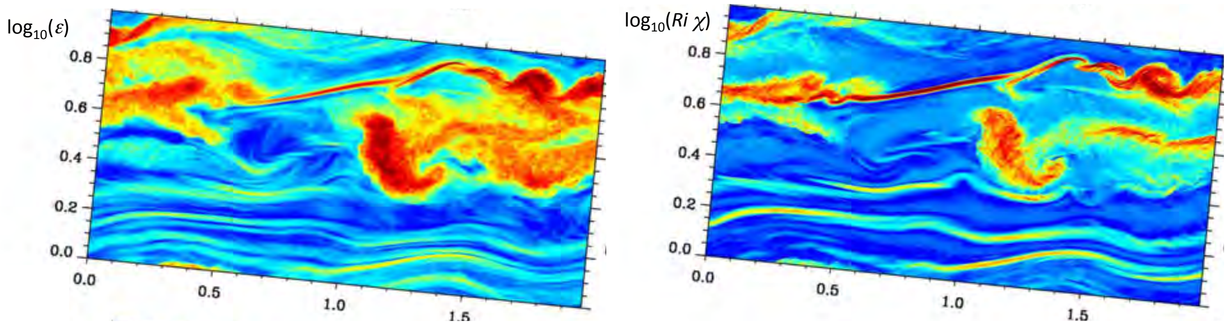

Figure 16. Spatial distributions of spanwise mean $\log_{10}(\varepsilon)$ and $\log_{10}(Ri\ \chi)$ (left and right) for the linear FS at t = 11.5 T_b. See the "voids" in $\log_{10}(Ri\ \chi)$ where $\log_{10}(\varepsilon)$ is large. Such regions have been inferred in related studies to suggest as loss of radar sensitivity in these regions.

7. Important Results Comparing Measurements and Modeling

7.1. New DNS Results

To enable detailed studies of multi-scale evolutions for comparisons with the DPG measurements, we have more recently performed new DNS of the linear fine-structure DNS discussed above at various *Re*, with the highest at *Re* = 100,000, twice that used by Fritts et al. (2013). The implications of higher *Re* for ε and Re_b are shown in Figure 17. This enables a broader inertial range of turbulence, and higher sustained ε and $Re_b = \varepsilon/\nu N^2$ ~25 during sustained turbulence, thus above the threshold for sustained small-scale turbulence in stratified flow of Re_b ~20. These results are reported by Fritts et al. (2014). In many respects, the new fields showing GWs, instabilities, and turbulence evolutions are very similar to those reported by Fritts et al. (2013) discussed above.

To compare these fields with the DPG measurements more directly, we mapped the fields from the DNS domain to a horizontal domain. Streamwise-vertical cross sections of the *u*, *w*, θ', and N^2 fields are displayed at t =10, 12, 14, and 16 T_b spanning the major instability evolutions in Figure 18. These are then sampled in a manner consistent with the DPG DataHawk sampling by Balsley et al. (2014).

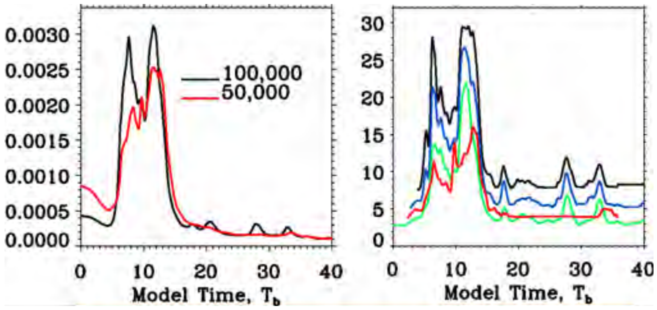

Figure 17. ε and Re_b (left and right) for *Re* = 50,000 (red) and 100,000 (different colors at right are for different thresholds of ε defining turbulent regions. For t ~6-14 T_b the flow is strongly turbulent, and ranges of ε scaled to the DPG SBL measurements are in close agreement with those values (after Fritts et al., 2014).

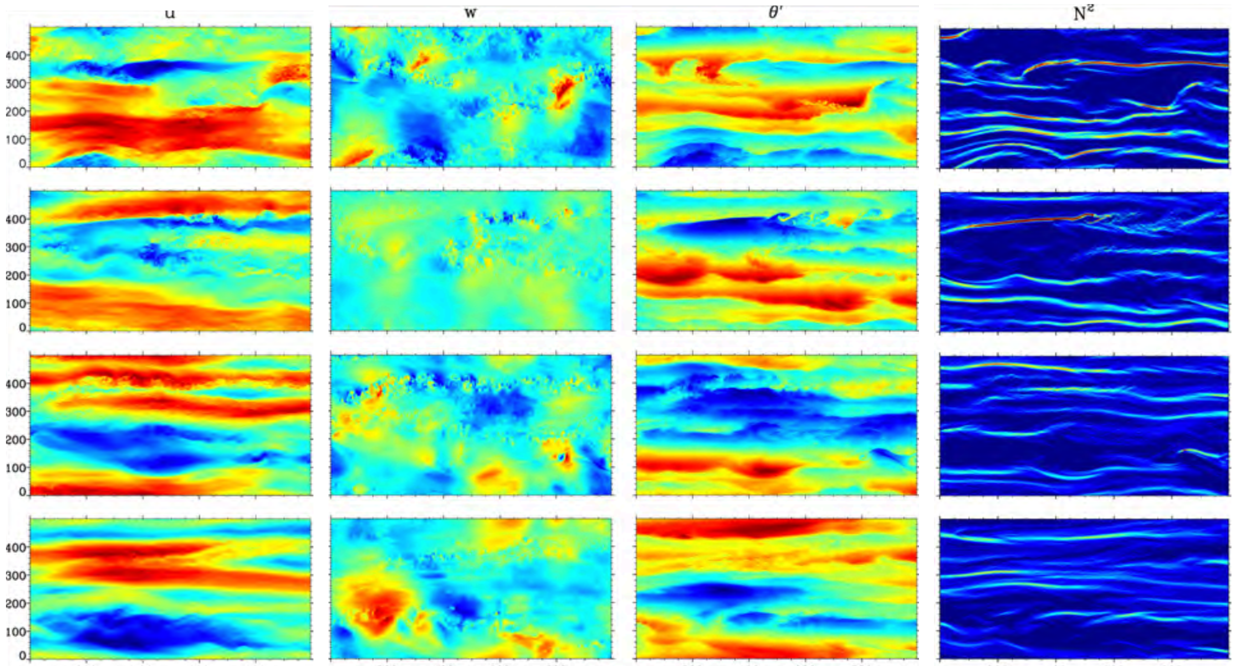

Figure 18. Streamwise-vertical cross sections of the *u*, *w*, θ', and N^2 fields at t =10, 12, 14, and 16 T_b for the DNS at Re = 100,000 (after Fritts et al. 2014). The fields are shown scaled to the DPG measurements (500 m deep and 1000 m long) for direct comparisons of measured and predicted fields.

7.2. Vertical and Slant-path Sampling

In order to interpret the small-scale dynamics observed by the DataHawk, we performed similar sampling of the DNS fields to those performed at DPG, both in the true vertical and along slanted streamwise paths having the same ascent and descent characteristics. A comparison of true vertical profiles at four horizontal locations and a representative slant-path profile displayed as a vertical profile (as in the DPG measurements in Figures 8-10) is shown in Figure 19. These reveal very similar overall characteristics to the DataHawk DPG measurements, but with higher spatial resolution along the slant-path track. Note, in particular, the S&L structures in θ, the larger-scale modulations of d', L_T, and log ε, and u and v.

Also shown by Balsley et al. (2014) are DNS perturbation fields along the true slant-path profiles for comparisons with the DPG measurements shown in Figure 11. Examples of these for the first three times are displayed in Figure 20. As described by Balsley et al. (2014), the DNS results enable association of the various correlations seen in the DPG measurements with specific small-scale GW and instability dynamics that provide key insights into the character of the observed SBL flow at DPG during these measurements. The primary small-scale dynamics contributing to turbulence events in both the DNS and the DPG measurements were found to be local KHI and GW breaking, suggesting that the canonical multi-scale DNS by Fritts et al. (2013, 2014) provide a reasonable approximation to more general SBL multi-scale flows.

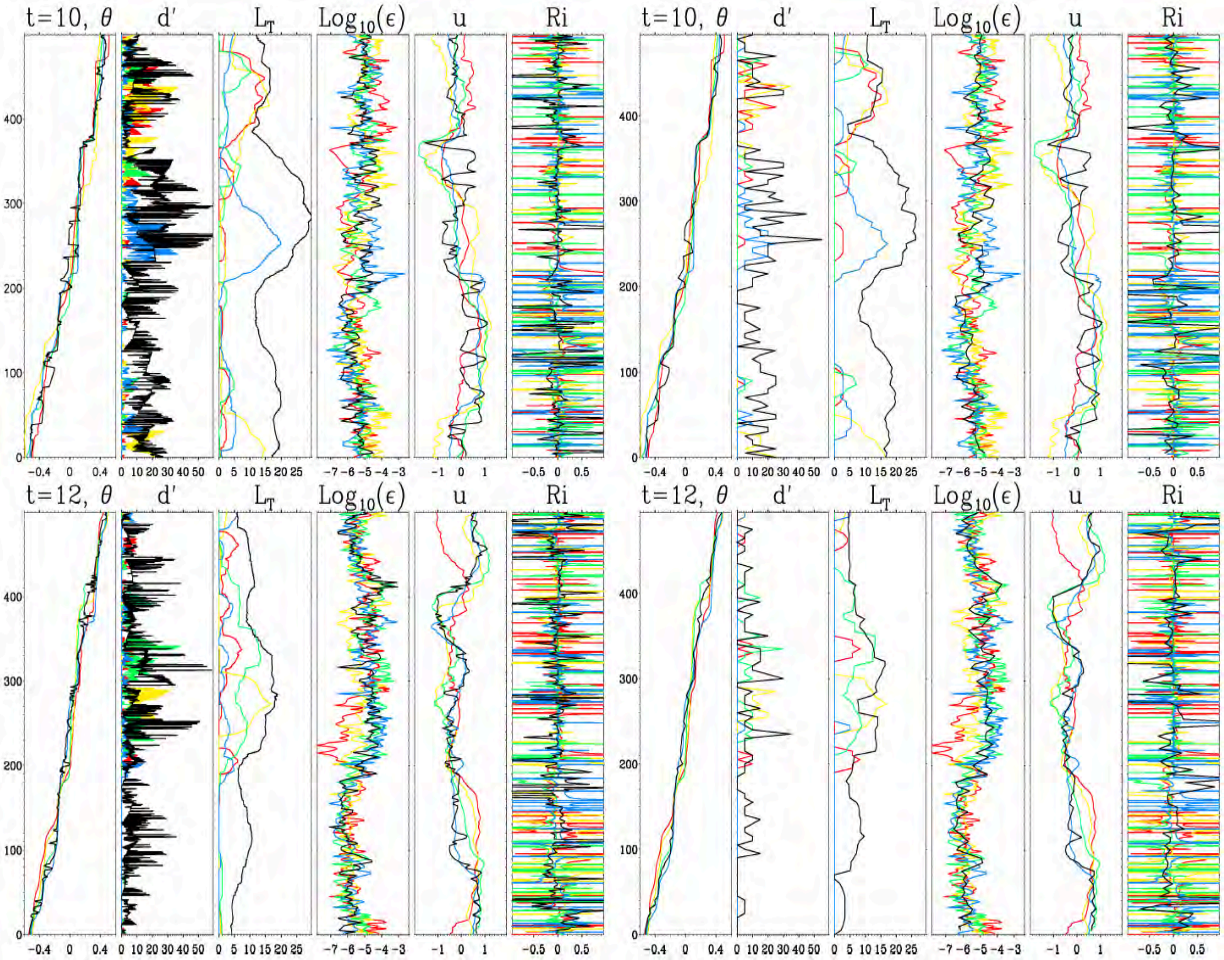

Figure 19. Vertical (colored) and slant-path (black) profiles of θ, d', L_T, log ε, u and v, and Ri from the DNS described by Fritts et al. (2014) and reported by Balsley et al. (2014).

8. Evaluation of the Thorpe/Ozmidov Scale Relation for Estimating ε

Our more recent DNS were also employed to assess the relation between the Thorpe and Ozmidov scales used by many in the atmospheric research and forecasting communities to estimate ε in the stably-stratified atmosphere (and oceans) from direct measurements of the Thorpe scale using high-resolution balloon data. The relation, $C = L_O/L_T \sim 0.8$ is commonly assumed. However, our DNS reveal that when C is evaluated for specific small-scale instability dynamics events, e.g., GW breaking, KHI, or fluid intrusions, C varies considerably among, and within individual events throughout the event evolutions. We also have shown why C is not a constant and developed statistics to shown the observed scatter in time, within groups of events having the same character, and among events of different character. It remains to be determined whether C ~0.8 can nevertheless be employed statistically to relate effective intermittent turbulence and mixing to the observed Thorpe scales for various stable atmospheric flows.

Comparisons of θ, N^2, ε, χ, Thorpe displacement d', L_T, and L_O computed in two ways are shown for a GW breaking event in Figure 21 and for a KHI event and a fluid intrusion in Figure 22. In each case, these show fields in sub-domains that are ~1/10th of the full domain that are averaged to provide estimates of the mean L_T, L_O, and C at each time. These estimates were also determined at several times for several events in each instability category. The same estimates were determined for the full domain as a function of time in a similar manner, and the results of both assessments are shown in Figure 23.

Estimates of C in Figure 23 are from 4-24T_b for the full domain (top) and with $\varepsilon > 0.01\varepsilon_{max}$ (dashed line). Semi-log distribution of C versus ε (bottom) for the individual events at each time (small text) and for the event means (large text). Numbers refer to events and numerals refer to sequential event times. Note in the top panel that the domain-mean C remains small as 3D energy is increasing (prior to 11.5T_b) and fluctuates between $C \sim 0.4$ and 2 or greater as instability and turbulence events subside.

The implications of these results are that C is not universal across event types, or within events at different times. However, there is some universality when averaged sufficiently over multiple events and times that may justify its use in an averaged manner.

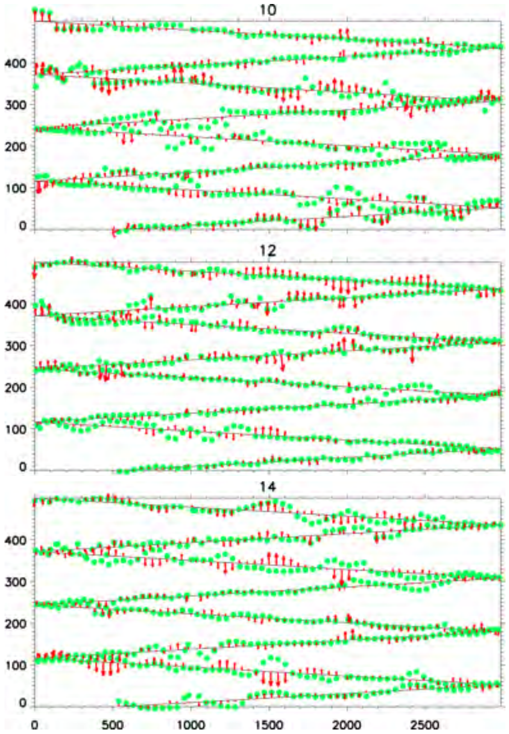

Figure 20. As in the DPG measurements shown in Figure 11, but from streamwise sampling of the DNS of Fritts et al. (2014). Times for the three panels at 10, 12, and 14 T_b.

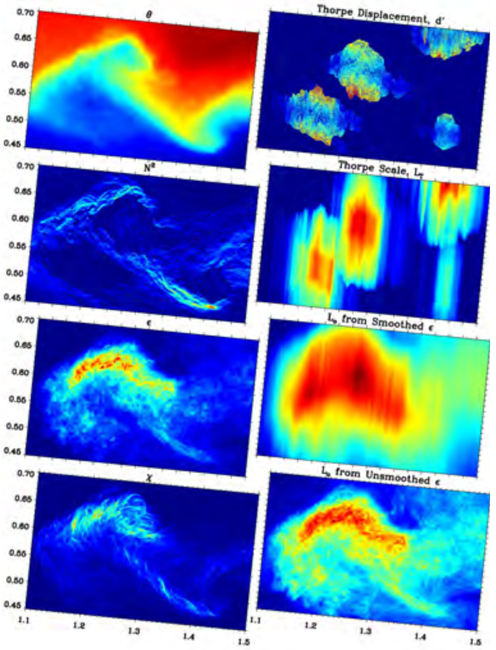

Figure 21. θ, N^2, ε, and $Ri\chi$ at left and d', L_T, and L_O assuming smoothed and local ε at right at t=11.1 T_b for a GW breaking event from Fritts et al. (2014).

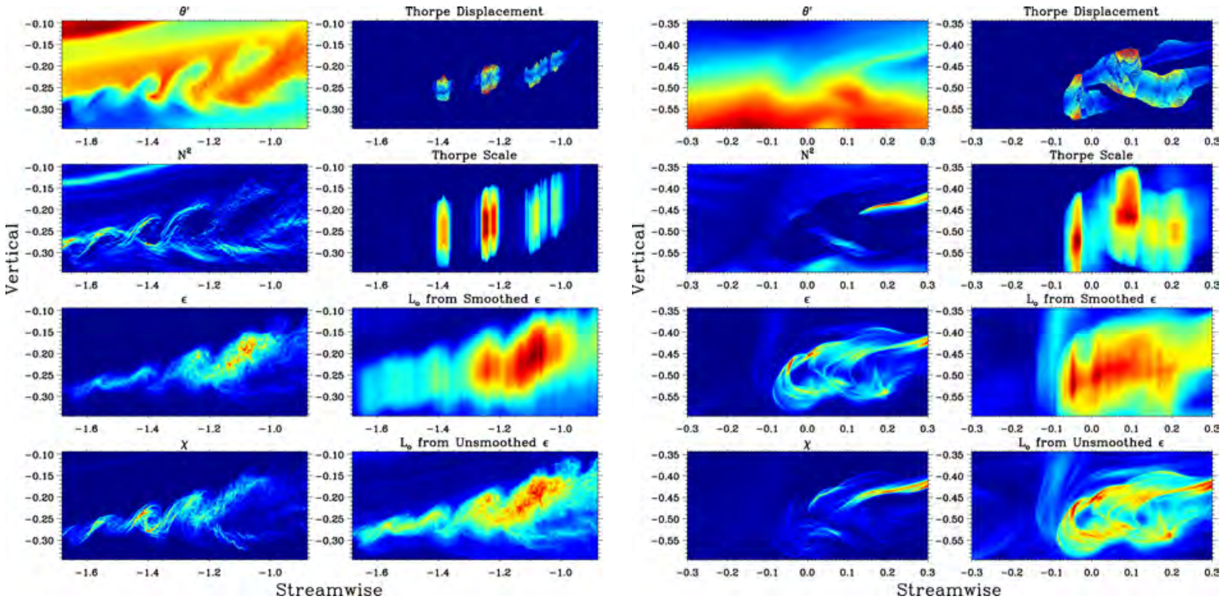

Figure 22. As in Figure 21 for a KHI event (left) and a fluid intrusion (right). (After Fritts et al. 2014). Similar assessments for these and other events were performed at various times throughout the various instability evolutions.

9. Bibliography: Publications Published, Submitted, and/or in Preparation

Balsley, B. B., D. A. Lawrence, D. C. Fritts, L. Wang, and K. Wan, 2014: Fine Structure, Instabilities, and Turbulence in the Stable Boundary Layer, Part 1: High-Resolution In-Situ Measurements with the DataHawk UAV and Comparisons with Numerical Modeling, J. Atmos. Sci., submitted.

Balsley, B. B., D. A. Lawrence, R. F. Woodman, and D. C. Fritts, 2013: Fine-scale characteristics of temperature, wind, and turbulence in the lower atmosphere (0-1300 m) over the south Peruvian coast, Bound. Layer. Meteorol., DOI 10.1007/s10546-012-9774-x.

Fritts, D. C., L. Wang, and J. A. Werne, 2013: Gravity Wave–Fine Structure Interactions. Part I: Influences of Fine Structure Form and Orientation on Flow Evolution and Instability. J. Atmos. Sci., 70, 3710–3734. doi: http://dx.doi.org/10.1175/JAS-D-13-055.1.

Fritts, D. C. and L. Wang, 2013: Gravity Wave–Fine Structure Interactions. Part II: Energy Dissipation Evolutions, Statistics, and Implications. J. Atmos. Sci., 70, 3735–3755. doi: http://dx.doi.org/10.1175/JAS-D-13-059.1.

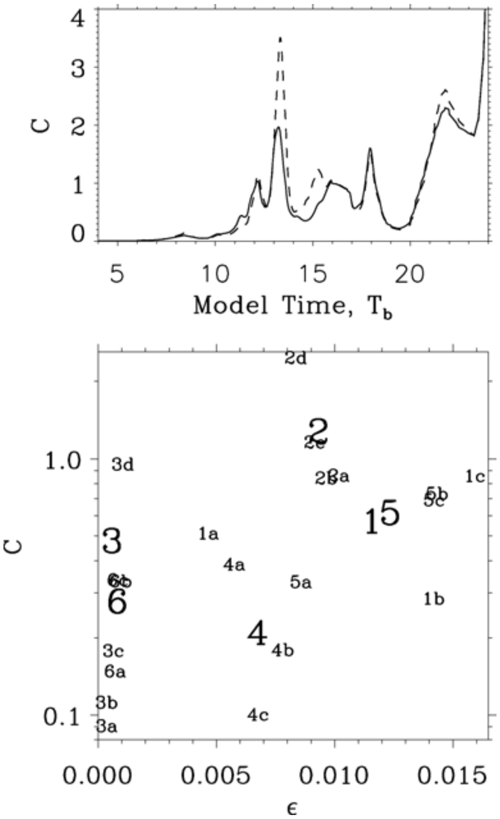

Figure 23. Estimates of C from 4-24T_b for the full domain (top) and for each instability event assessed (see text for details). (After Fritts et al., 2014).

Fritts, D. C., G. Baumgarten, K. Wan, J. A. Werne, T. Lund, 2014a: Quantifying Kelvin-Helmholtz Instability Dynamics Observed in Noctilucent Clouds: 2. Modeling and Interpretation of Observations, J. Geophys. Res., 119 (15), 9359-9375.

Fritts, D. C., L. Wang, and M. A. Geller 2014c: Instability and Turbulence Dynamics in Multi-Scale Flows: Relations between the Ozmidov and Thorpe Scales and Dissipation Fields in a Direct Numerical Simulation. J. Geophys. Res., to be submitted.

Fritts, D. C., L. Wang, K. Wan, M. A. Geller, D. A. Lawrence, J. Werne, and B. B. Balsley, 2014b: Fine structure, instabilities, and turbulence in the stable boundary layer, Part 2: Numerical modeling of multi-scale interactions, instabilities, and turbulence, J. Atmos. Sci., submitted.

Wang, L., D. C. Fritts, and M. A. Geller, 2014d: On the Reynolds number dependence of small-scale instabilities and turbulence in multi-scale flows, to be submitted.